www.sciencemag.org/cgi/content/full/science.aav3932/DC1

Supplementary Materials for

Thirst regulates motivated behavior through modulation of brainwide neural population dynamics

William E. Allen, Michael Z. Chen, Nandini Pichamoorthy, Rebecca H. Tien, Marius Pachitariu, Liqun Luo*, Karl Deisseroth*

*Corresponding author. Email: lluo@stanford.edu (L.L.); deissero@stanford.edu (K.D.)

Published 4 April 2019 on *Science* First Release
DOI: 10.1126/science.aav3932

This PDF file includes:

Other supplementary material for this manuscript includes:

Materials and Methods

Mice

All animal procedures followed animal care guidelines approved by Stanford University's Administrative Panel on Laboratory Animal Care (APLAC) and guidelines of the National Institutes of Health. The investigators were not blinded to the genotypes of the animals. Female mice from a wildtype (*C57BL6/J*), or *Nos1-Cre* (*BG.129-Nos1$^{tm1(CreMgmj)}$/J*) background were used for experiments, aged 6–12 weeks at the time of surgery. Animals were maintained on a reverse 12 hr dark/12 hr light schedule, and experiments were performed during the dark period. Data from 21 mice (14 wildtype, 7 *Nos1-Cre*) were included in this study. Mice were water restricted starting ~1 week before the onset of training to ~1 mL per day, which was obtained during task performance once training began. There was no randomization or blinding of experimental treatments. The sample size was set based on conventions in the field.

Surgeries

For all surgeries, mice were anesthetized with 1–2% isoflurane, and sterile techniques were utilized. Mice were given sustained-release buprenorphine (1 mg/kg) prior to surgery. Mice were stereotaxically affixed, the scalp and periosteum was removed, and the skull was cleaned with hydrogen peroxide and saline. After allowing the skull to dry, possible recording locations were stereotaxically marked with a permanent marker (frontal cortex: +2.2 A/P, 1.5 M/L; ventral striatum: +1.4 A/P, 1 M/L; mPFC: +1.9 A/P, 0.3 M/L; dorsal thalamus: –0.7 A/P, 0.1 M/L; LH: -1.3 A/P, 1.1 M/L; amygdala: -1.5 A/P, 3.3 M/L; dorsal striatum: 0.25 A/P, 2 M/L; midbrain: -3.5 A/P, 1 M/L; lateral cortex: +1.6 A/P; 2.7 M/L). These recording locations were chosen in part based on preliminary retrograde tracing experiments from several brain regions thought to be involved in thirst (including paraventricular thalamus, lateral hypothalamus, nucleus accumbens, and mPFC) that implicated a large, recurrently connected network of many regions throughout the brain. A headbar was then affixed over the cerebellum with dental cement, and the exposed skull was protected with clear UV curable glue. Mice were allowed two weeks to recover before behavioral training. Prior to recording, a platinum/iridium reference electrode (~2 mm long, insulated except for the last ~200 μm) was implanted into the posterior aspect of the skull (approximately over visual cortex) on the contralateral hemisphere from the side being recorded.

In the *Nos1-Cre* mice, an additional step was performed prior to headplate implantation to allow optogenetic stimulation of subfornical organ (SFO) neurons. AAV5-EF1a-DIO-ChR2-eYFP (350 μl of ~5 x 10^{12} vg/mL titre) was injected into SFO (-0.5 M/L, 0 M/L, -2.75 D/V relative to bregma) at 100 nl/min with a Hamilton syringe, then 10 min were allowed to elapse before removing the syringe. A 400 μm fiber optic with 1.25 mm cannula was then implanted over the SFO at a 30^{o} angle (-0.5 A/P, +1.4 M/L, -2.76 D/V) and held in place with dental cement.

Histology

Mice were perfused with phosphate-buffered saline and 4% paraformaldehyde, and brains were postfixed overnight at 4^{o}C. For regular histology, brains were sectioned at 60 μm on a vibratome and imaged on a confocal microscope.

For intact brain clearing, since no labeling of biomolecules was required nor was retention of any native fluorescence signal needed, the more powerful hydrogel-tissue chemistry methods were not required and brains were simply sequentially dehydrated in a

methanol gradient (20%, 40%, 60%, 80%) for 1 hr each at room temperature and bleached overnight at 4°C in a mixture of 5% hydrogen peroxide in ice-cold methanol. Brains were then washed twice at room temperature for at least 1 hr in 100% methanol to remove any residual water, and transferred to a mixture of 67% dichloromethane/33% methanol for at least 3 hrs to overnight with shaking. Finally, the brains were washed twice for 15 min each time in 100% dichloromethane, and transferred to 100% dibenzyl ether overnight. Brains were stable in dibenzyl ether indefinitely.

Whole-brain Imaging and Registration

Cleared brains were imaged on a LaVision lightsheet microscope in dibenzyl ether at 488 nm (green autofluorescence) and 532 nm (electrode tracks labeled with CM-DiI a fixable, lipophilic red dye that is stable even when dehydrated) with 4 µm step size, ~4 µm pixel size (0.8X magnification), and a single light sheet focus. Only the hemisphere with electrode tracks was imaged, in a sagittal orientation.

The green and red channel images were then downsampled with averaging to 25 µm resolution. The green channel was then registered to the Allen Brain Atlas CCFv3 autofluorescence atlas at 25 µm resolution using an affine transform followed by a non-linear transform implemented in Elastix, which was previously shown to have an average registration error of 4 voxels (100 µm) (*46–48*). This transformation was then applied to the red channel, and the electrode tracks were traced in the registered space using custom MATLAB software, built on AllenCCF (https://github.com/cortex-lab/allenCCF). Electrophysiological recordings were targeted stereotaxically to specific brain regions, and each insertion was at least several hundred microns away from any other insertion, which allowed for unambiguous determination of which insertion corresponded to which recording sessions based on the particular set of brain regions penetrated by that insertion. In this way, we could identify many different insertions in the same animal. For the final analysis, brain regions were grouped based on the Allen Brain Atlas hierarchy into 34 distinct regions. Unit locations were determined based on the location of the electrode where that unit had the highest amplitude. The electrodes are spaced 25 µm apart (center to center). This location along the electrode was transformed into the Allen Brain Atlas space based on the orientation and position of the traced electrode track for that recording.

Behavioral Training

Mice were trained on a behavior rig using a two-odor olfactometer, an optical lickometer, and behavioral protocols controlled in real-time by an Arduino (Bpod). Mice sat in a clear plastic tube in front of the lickometer and olfactometer. Pure odorants (ethyl acetate and 2-pentanone) were diluted to 4% v/v in mineral oil. A pure stream of air flowed through the olfactometer between odor delivery. Mice were water restricted for approximately one week prior to training, trained to lick for water while headfixed, then shaped to lick for water reward (~3 µl) on the Go odor by automatically delivering a water droplet during the reward period (2–3 s after odor onset) on every Go trial. No-Go trials were always unrewarded. After 4.1 s from the start of the trial, there was an exponentially distributed inter-trial interval (ITI) with mean duration 2 s. After mice were proficient at licking for the automatically delivered reward, and began to lick in anticipation of this reward (1–3 days), they were moved to the training protocol in which reward delivery was contingent on them licking during the reward period. Mice were then trained on this protocol until they obtained rewards on > 85% of Go trials (2–5 days).

After the beginning of water restriction, mice received all their daily water (~1 mL) by performing the task.

Electrophysiological Recordings

At least three hours prior to the recording, the mice were briefly anesthetized, a small (<1 mm) craniotomy was made over a pre-marked location, and the dorsal skull was covered with Quik-Cast. Mice were then allowed to recover in their homecage until the time of recording. At the time of recording, mice were headfixed and put on the recording apparatus. The Quik-Cast was removed, and a pool of saline was put into a well built into the headbar to keep the craniotomy moist. Recordings were performed using Phase 3A, Option 1 (5 mm, passive) or 3 (1 cm, passive) Neuropixels electrodes (*5*) with 374 active recording sites (out of 960 total) along the bottom ~4 mm of a ~10 mm shank (70 μm wide shank diameter, 20 μm thick, 25 μm electrode spacing), and reference and ground shorted together. A few minutes prior to recording, the electrode was coated with a red fixable lipophilic dye (CM-DiI, Thermo Fisher) and allowed to dry. The electrode reference was then connected to a chronically implanted reference electrode on the skull with a gold pin, was then positioned over the craniotomy with a micromanipulator. The electrode array was slowly (~20 μm/s) advanced 4–5 mm into brain while being observed under a stereomicroscope for bending or bleeding. The array was allowed to sit in the brain for 15 min, and then recording began. Signals were sampled at 30 kHz with gain = 500 (2.34 μV/bit at 10 bit resolution) in the action potential band, digitized with a CMOS amplifier and multiplexer built into the electrode array, then written to disk using SpikeGLX software. Mice were then allowed to perform the task until they became sated, at which point a few dozen more trials were recorded. For optogenetic stimulation trials, after the sated trial block, a 488 nm laser (~20 mW at fiber tip) was used to stimulate for 1 s at 20 Hz with 20 ms pulse width in a raised cosine pattern every 4th second. This stimulation was unsynchronized with task, and was turned on for ~2–5 min before recording the stimulation block of trials, and was turned off for ~2–5 min before the washout block of trials. The session start times, trial start times, and stimulation times were recorded on a separate data acquisition board, along with a synchronization signal that was simultaneously recorded by the Neuropixels and used to correct slight drift between the acquisition computer clock and Neuropixels FPGA clock. All recordings were completed within ~1–1.5 hrs. Between recordings, the skull was protected with Kwik-Cast.

Spike Sorting

Data from the Neuropixels action potential band were first common average referenced to the median across channels (*24*), and high-pass filtered above 150 Hz. Spike sorting was performed offline using Kilosort2 (*25*), a high-throughput spike sorting algorithm that tracks clusters that drift over time and automatically determines the number of clusters.

Like Kilosort1 (*49*), Kilosort2 is a template-based algorithm that determines for each cluster an average template shape. It then matches this template to the raw voltage data to find matches, and subtracts these matches iteratively using a matching pursuit algorithm. To account for slow timescale changes in the cluster shapes, Kilosort2 allows the templates to change as a function of time. Kilosort2 processes data batches in temporal order, and continually re-estimates the cluster templates as the running average of the past ~400 spikes, using an exponential filter with decay constant 200. To account for potentially fast drift, Kilosort2 has an initial step in which it re-orders data batches such that nearby batches have similar levels of drift. After the reordering, it proceeds

through the batches in order like before. If only slow drift dominates a recording, the reordering does not modify the temporal order in which Kilosort2 processes the data. To further increase robustness to drift, Kilosort2 automatically merges clusters with nearly-overlapping distributions of spikes (as determined by a mean and standard deviation criterion). To ensure that all large spikes are assigned to a cluster, Kilosort2 continually evaluates the data residual and introduces new templates to account for un-matched, large threshold crossings. If these new templates are determined to be continuous with an existing template, they are merged together, again increasing the robustness to drift.

After sorting, clusters with a peak-to-peak signal-to-noise ratio of < 2.5 or an average firing rate of < 0.02 spike/s over the whole recording were removed. The clusters were manually validated using Phy (*50*) to determine whether they were "Good" (well-isolated and stable over time) or "Noise" (poorly or unstable isolated units and electrical artifacts) (similar to the instructions here:

https://phy-contrib.readthedocs.io/en/latest/template-gui/).

A convolutional neural network-based classifier, using spike waveform and autocorrelogram shape as inputs, was developed based a subset (~10%) of this manually-curated data to assist in identifying "Noise" clusters, and then applied to all subsequent recordings. All units not classified as "Noise" were then manually inspected, and clusters with high signal-to-noise ratio, clean spike time autocorrelograms (few refractory period violations), and no significant drift in waveform amplitude over time were classified as "Good" (i.e., putative single units). All other clusters, including multi-unit activity, were classified as "Noise" and not analyzed.

Electrophysiological Data Analysis

Spike trains were aligned to the trial start and binned at 10 ms resolution for analysis. The brain region each unit resided in was determined by finding the location of the channel with peak amplitude for that unit on the electrode array, and then transforming that location into Allen Brain Atlas space.

For all analyses, we excluded rare Miss and False Alarm trials while thirst, and Hits and False Alarms during the sated block. Therefore, in all figures 'thirsty Go' = Hits during thirsty block, 'thirsty No-Go' = Correct Reject during thirsty block, 'sated Go' = Miss during sated block, 'sated No-Go' = Correct Reject during sated block. Thirsty and sated blocks were determined using a Hidden Markov Model of the total number of licks per Go trial, smoothed with a 10 trial moving average filter.

For visualization of per-cell average firing rates, trial-averaged firing rates were smoothed with a 50 ms Gaussian filter, the average firing rate within the baseline period was subtracted per condition, and then the average rates were normalized to the min and max firing rate across all conditions.

For computing average activity for visualization of per-neuron and per-region firing rate (Fig. 2), at most 30 trials were randomly sampled from the entire trial block (e.g., 30 trials each were randomly from thirsty Go trials, 30 sated Go trials, etc.) A similar number of trials was taken from the stimulation and washout blocks. For computing average activity within different parts of the session (Beginning, Middle, End, Sated), the first 20 trials of the thirsty block, middle 20 trials, and last 20 trials were taken, along with 20 trials while the animal was sated. To consistently average trials with the same behavior in different trial blocks, False Alarm and Miss trials were excluded from this analysis when the animal was thirsty, as were rare Hit trials while the animal was sated.

Task-modulated cells were identified based on a Wilcoxon rank-sum test of average firing rate within the 1 s baseline and three sequential 1 s epochs within the task starting at the odor onset, on a per trial basis. A cell was deemed task modulated if any of the task epochs differed significantly from the baseline after false discovery rate (FDR) correction across all units, with a corrected significance threshold of $P < 0.001$.

Single-cell Analysis

Trial-averaged firing rates for task-modulated cells were z-scored across conditions (thirsty/stated x Go/No-Go), principal components analysis was applied to the cellular activity across all trial conditions, and then clustered using shared nearest neighbor graph-based clustering (*51*) on the top 20 PCs. The number of clusters was automatically determined by the clustering algorithm.

For the encoding analysis, per-cell firing rates were averaged to 20 ms resolution, and smoothed with 100 ms Gaussian filter. The predictors used were 'ITI' (3.2 s long), 'Go odor onset' (1 s), 'No-Go odor onset' (1 s), 'Go odor offset' (1 s), 'No-Go odor offset' (1 s), 'lick times' (0.25 s around each lick), 'lick onset' (0.5 s), and 'reward' (0.75 s), and 'Thirsty' (6 s). For all predictors except 'Thirsty', the predictors were raised cosines, repeated ten times the length of the event, and spaced such that each raised cosine was 1/4 the width of each cosine. The 'Thirsty' predictor was a constant value that spanned the entire trial, and was high when the animal was thirsty and low when it was sated. Predictors were then constructed for each trial. These predictors were then used to fit a model for each cell that attempted to predict the trial-by-trial firing rate. The predictors were maximum-normalized and z-scored before fitting. To fit these models, we used XGBoost (*52*), a highly efficient machine learning algorithm that uses gradient boosting for classification and regression, with a Poisson loss function. For training and testing, the data were split into alternating trials; half the data was then used to fit the model, and the other half was used for testing. The goodness of fit was evaluated in terms of the fraction of explained deviance: $DE = 1 - D_{model}/D_{null}$, where D_{null} is the deviance for a null model that predicts the cell's average firing rate at all timepoints, and D_{model} is the model deviance (*53*, *54*). Poisson deviance was computed as $2\sum y \log(y/\hat{y}) - y + \hat{y}$, where y is the true firing rate across all trials, and $\hat{y}$ is the predicted firing rate.

To determine the per-feature DE, we shuffled the values for each regressor across time individual (while keeping all the other regressors unshuffled), refit the model on training data, and evaluated the DE on held-out test data (*55*). The unique DE by that variable was then computed as the difference between the DE by the full model and DE by the model with that regressor shuffled.

To determine the total DE by sensory features, we summed the unique deviance explained of 'Go odor onset' and 'No-Go odor onset'. To determine the total DE by motor features, we summed the unique DE by the 'lick times', 'lick onset', and 'reward' features.

To determine which features or combination of features modeled individual cells well, we used a simple threshold of 4% deviance explained for each feature.

Activity Mode Analysis

To determine different activity modes within the data, we used a variant of the 'Coding Direction' analysis described in (*34*). We first subtracted the per-cell mean activity across all conditions (thirsty/sated or thirsty/sated/stim/washout). We then computed different directions in activity space that would optimally separate different task events, by taking the difference in mean population activity between different trial

conditions within different epochs. All recorded neurons (i.e., both task-modulated and non-task-modulated neurons) were used in computing these modes and visualizing projections onto them. The 'State mode' was computed as the average difference between thirsty and sated trials in the baseline epoch (1 s before odor onset), and then averaged across that 1 s interval. Specifically, the average baseline period of at most 40 randomly thirsty Go trials were contrasted with the weighted sum of average baselines of at most 40 randomly selected sated Go (67%) and No-Go trials (33%), to ensure a robust estimate in spite of there always being fewer sated trials of any type. Since the baseline period contained no task-related behavior or sensory input, we found that the trial type label (Go vs No-Go) was irrelevant, and these subsets of trials were chosen for convenience; other subsets yielded equivalent results. The 'Cue mode' was computed as the average difference in per-cell activity between thirsty Go and No-Go trials, from at most 40 randomly subsampled trials of each type, in the odor epoch (0.5 s after odor onset [before licking onset]), and then averaged over time within that window. Finally, the 'Behavior mode' was computed for the same trials, but using the response epoch (1 s around the 2 s after odor onset [approximate time of reward on thirsty Go trials]). For a population of N neurons, this yielded three $N \times 1$ vectors. QR decomposition was then applied to these vectors to form three orthogonal axes $\mathbf{W}$, an $N \times 3$ matrix. Trial averaged data was then projected onto these axes using as the dot product as $\mathbf{W}^{\mathrm{T}}\mathbf{x}$, where $\mathbf{x}$ is an $N \times (4 \times T)$ matrix of smoothed, trial-average firing rates across 4 conditions (thirsty/sated x Go/No Go) concatenated together (T=600 10 ms bins each). For single-trial analysis, only populations where >20 neurons were recorded simultaneously from a single brain region were used. The different axes were similarly computed from trial averaged data within that population, but then single trials firing rates matrices of size $N \times T$ were projected onto them. For visualization, the absolute value of the separation between the trial averages of these projections were shown: for the per region projections onto the State axis, this was $|\langle\text{Thirsty}\rangle - \langle\text{Sated}\rangle|$, and for the Cue and Behavior axes, this was $|\langle\text{thirsty Go}\rangle - \langle\text{thirsty No-Go}\rangle|$, where $\langle \cdot \rangle$ indicates the average across that trial condition, and $|\cdot|$ is the absolute value. The axes were always fit only on thirsty and sated trials.

Decoding Analysis

Decoding of categorical variables (satiety state and trial type) was performed using regularized linear discriminant analysis, with shrinkage analytically determined from the covariance matrix. Firing rates from simultaneously recorded neurons within a brain region were averaged to 100 ms resolution, and analyzed without smoothing. Only populations of at least 20 neurons recorded simultaneously were analyzed. Decoding of continuous variables was performed using regularized linear regression, also setting the hyperparameter through cross validation. Decoding of satiety state was performed on the 1 s prior to odor onset, and data from the entire session (thirsty + sated) was split into alternating trials so that the decoder was trained on one half of the data and tested on the other half. Decoding of trial type was performed on the first 0.5 s after odor onset, and was only trained on half of the trials from the thirsty state. Finally, decoding of per-trial number of licks was performed on the 1 s around 2 s after odor onset, and data from the entire session (thirsty + sated) was split into alternating training and test trials.

When analyzing stimulation and washout trials, 40 trials from the end of the thirsty block and the sated block were used for training (with a 50:50 test/train split as described above), and then held out thirsty, sated, stim, and washout data were used for testing.

For comparing size-matched decoders, the minimum population size was subsampled from the total population 100 times without replacement. The decoder was trained as described above on each subsampled population, and the predictive accuracy was averaged for that particular recording.

For determine chance levels of decoding accuracy, the total population from each recording was trained on in the same was as described above, but the training data were first shuffled on a per-trial basis. This procedure was repeated 100 times per recording, and the mean results were compared with the mean decoding accuracy from the unshuffled data.

Data Availability

Data analyzed in this study are available online at http://clarityresourcecenter.org.

Open-Source Software Acknowledgements:

We would like to acknowledge the following open source software that was used for data analysis:

- SciPy: Jones E., Oliphant E., Peterson P., et al. SciPy: Open Source Scientific Tools for Python (2001). (https://www.scipy.org/)
- Numpy: Oliphant E. A., Guide to NumPy, USA: Trelgol Publishing, (2006). (http://www.numpy.org/)
- Matplotlib: Hunter J. D., Matplotlib: A 2D graphics environment, *Computing In Science & Engineering* (2007). (https://matplotlib.org/)
- Scikit-learn: Pedregosa, et al., Scikit-learn: Machine learning in Python, *JMLR* **12**, 2825-2830 (2011). (http://scikit-learn.org/stable/)
- Pandas: McKinney W. Data Structures for Statistical Computing in Python, *Proceedings of the 9th Python in Science Conference*, 51-56 (2010). (https://pandas.pydata.org/)
- IPython: Perez F., Granger B.E. IPython: A System for Interactive Scientific Computing**,** Computing in Science & Engineering, **9**, 21-29 (2007). (https://ipython.org/)
- Seaborn: https://seaborn.pydata.org/
- Statsmodels: Skipper S., and Perktold J. Statsmodels: Econometric and Statistical Modeling with Python, *Proceedings of the 9th Python in Science Conference (*2010)
- Keras: https://keras.io/
- AllenCCF: https://github.com/cortex-lab/allenCCF
- Spikes: https://github.com/cortex-lab/spikes
- SpikeGLX: https://github.com/billkarsh/SpikeGLX
- Kilosort2: https://github.com/MouseLand/Kilosort2

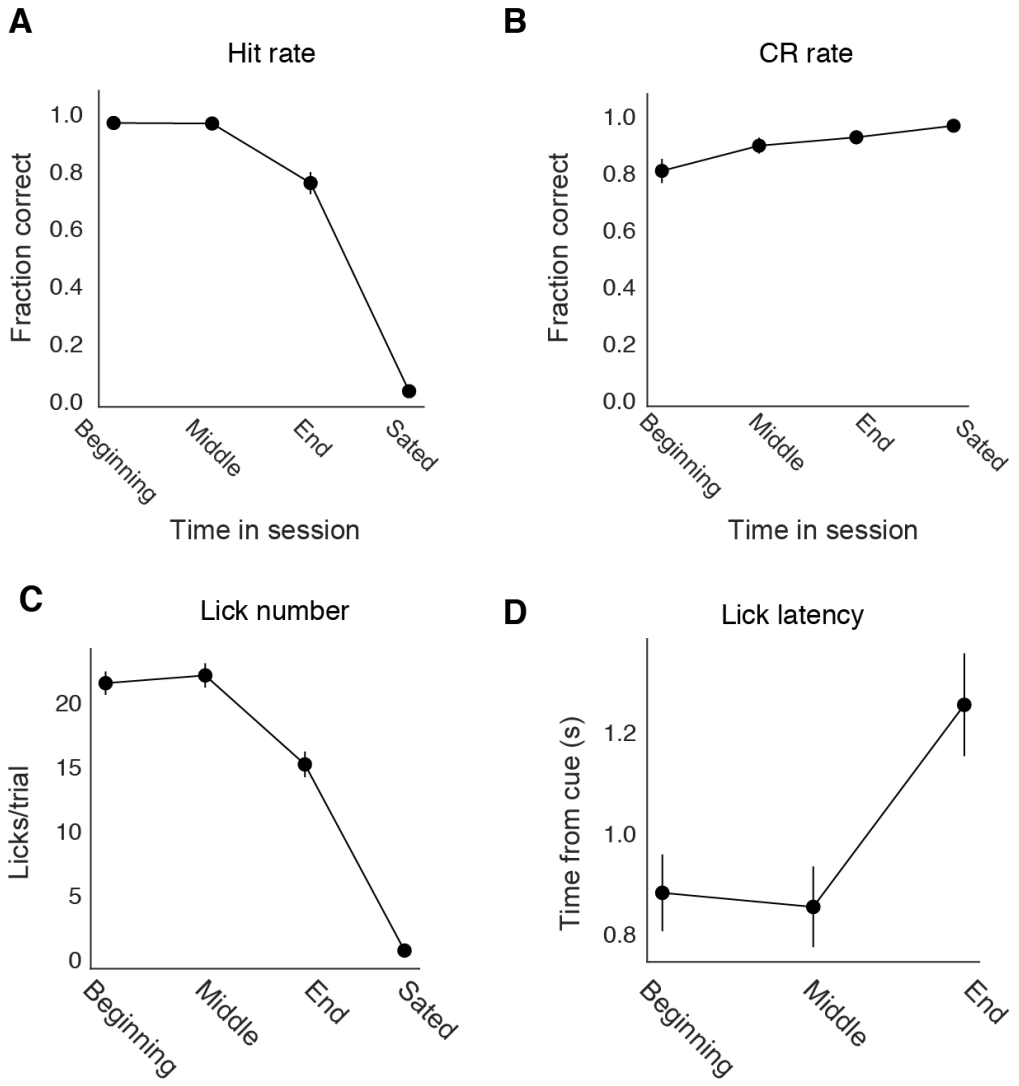

Fig S1: Extended behavioral data. (**A,B**) Hit rate and Correct Rejection (CR) rate at beginning (first 30 trials), middle (middle 30 trials), and end (last 30 trials) of thirsty session, and while sated. (**C**) Total number of licks per trial on Hit trials at different points in session. (**D**) Latency to first lick on Hit trials at different points in session. Mean ± 95% c.i.

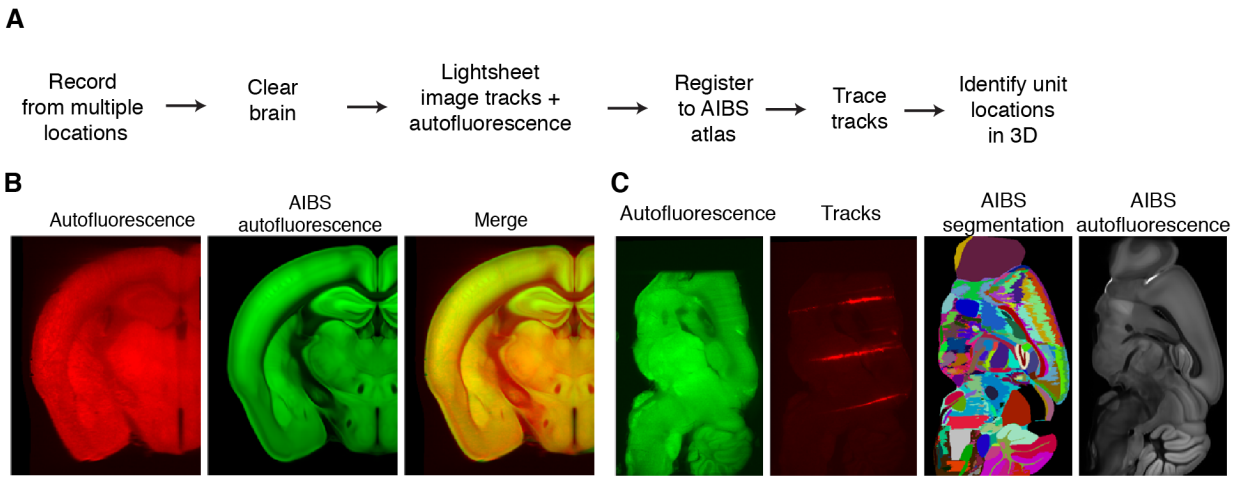

Fig S2: 3D registration of electrode tracks. (**A**) Diagram of experimental pipeline for electrophysiological recordings, brain clearing, and registration. (**B**) Example coronal section from brain post registration showing overlay between sample autofluorescence and Allen Brain Atlas autofluorescence. (**C**) Example sagittal section from brain post registration, showing autofluorescence, multiple fluorescent electrode tracks, and Allen Brain Atlas brain region segmentation and autofluorescence used for registration. Tracks are labeled with a red fluorescent, fixable lipophilic dye coated on the electrode prior to recording.

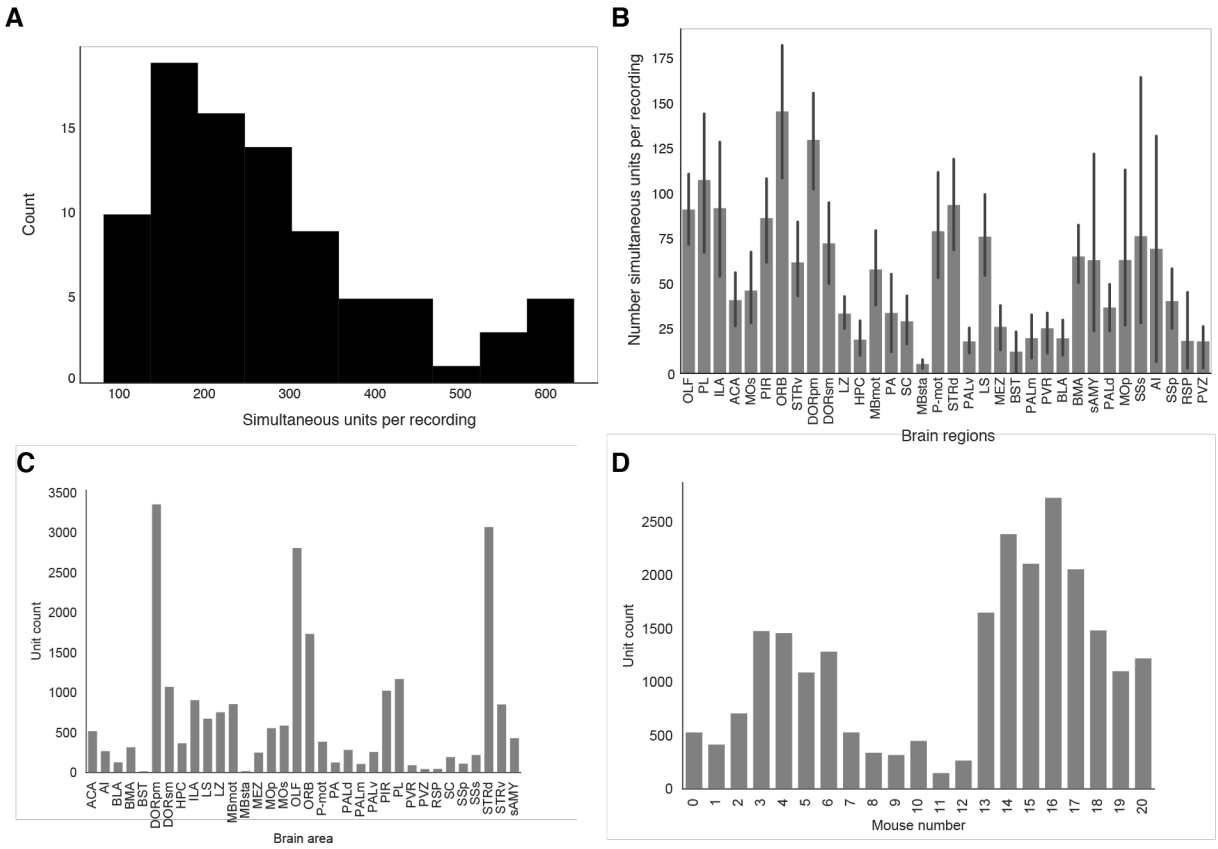

Fig S3: Recording statistics. (**A**) Number of simultaneously recorded neurons per recording session. (**B**) Number of simultaneously recorded neurons per brain region. Mean ± 95% c.i. Number of recording sessions per region: OLF=27, PIR=11, SSp=3, SSs=3, BLA=3, BMA=5, sAMY=6, PA=3, DORpm=22, DORsm=14, PVR=3, PVZ=2, LZ=15, MEZ=6, HPC=8, STRd=24, STRv=11, LS=9, PL=9, ILA=8, ORB=12, ACA=10, AI=2, RSP=2, PALd=6, PALm=3, PALv=5, BST=2, MOp=6, MOs=9, SC=3, MBmot=11, P-mot=5. (**C**) Total number of units recorded from each brain region. (**D**) Total number of units recorded from each mouse.

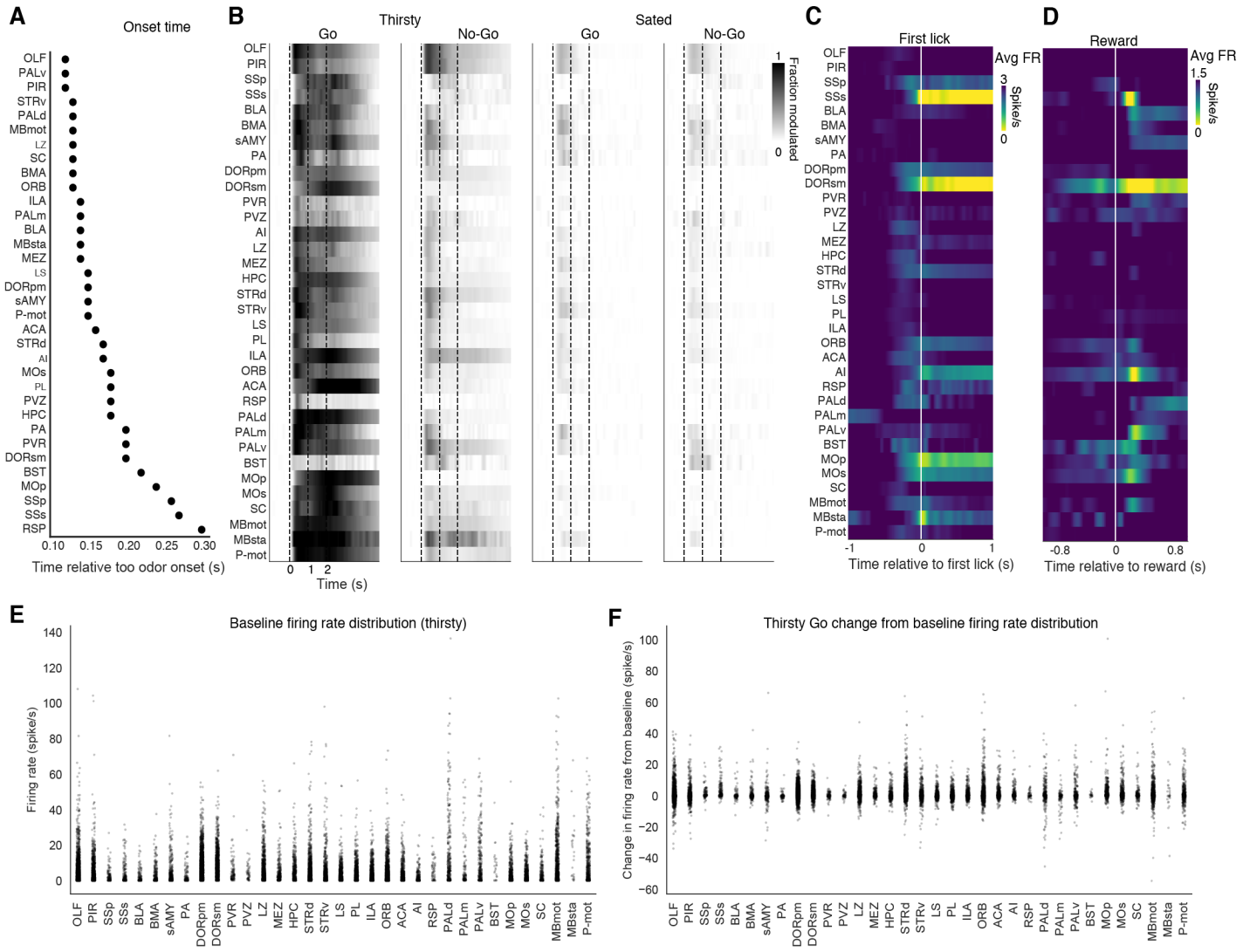

Fig S4: Extended data on population activity. (**A**) Regions sorted by Onset Time, defined as the first time bin at 10 ms resolution wherein the average firing rate of at least 5% of recorded neurons from that region is statistically different from baseline; note this is to be distinguished from peak time. 10 ms bins. Statistically different is defined as $P < 0.01$, two-tailed paired t-test of firing rate in each bin relative to average firing rate before odor onset, Bonferroni corrected across all timepoints. (**B**) Fraction of neurons statistically significantly different from baseline per region over trial on thirsty and sated Go and No-Go trials. (**C**) Average population firing rate per brain region aligned to first lick per trial, normalized to the 1 s before lick onset. (**D**) Average population firing rate aligned to reward time, normalized to the 1 s before reward, sorted as in (C). For (C) and (D), no regions had decreases in firing rate, so only positive values are shown. (**E**) Distribution of average pre-stimulus baseline firing rates per brain region during thirsty block. (Each dot is one neuron.) (**F**) Distribution of average change in firing rate during Go odor cue in thirsty block.

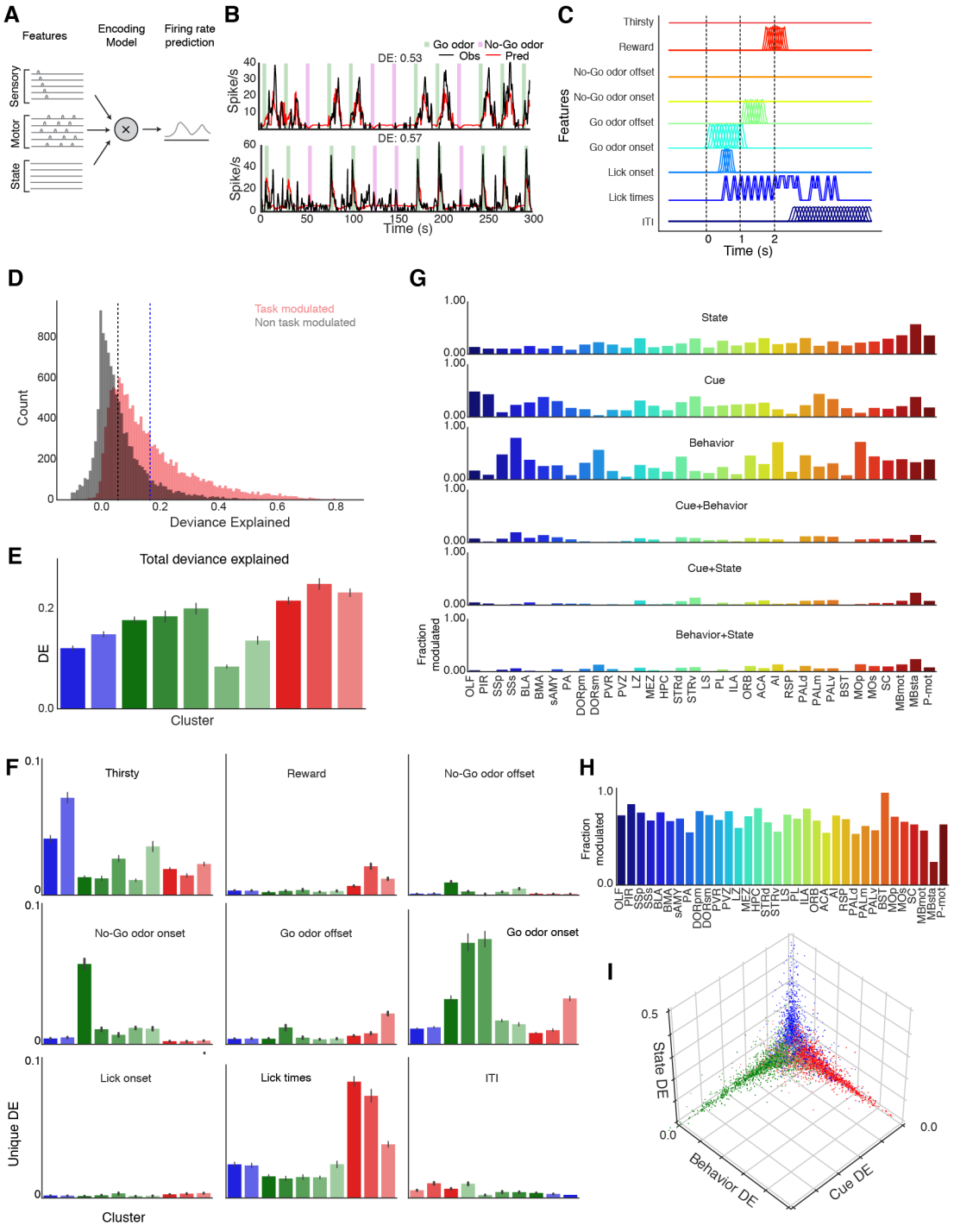

Fig S5: Extended data on single-neuron modeling. (**A**) Diagram of feature-based modeling of neuronal activity. Different features are combined to predict the firing rate of individual neurons on held-out test data. (**B**) Two example neurons, showing odor times (magenta and green bars) and observed (Obs) vs predicted (Pred) firing rates across multiple trials. DE = ratio of Poisson deviance explained in observed data by model. Top: a neuron from PALv (ventral pallidum). Bottom: a neuron from PIR (piriform cortex). (**C**) Examples of regressors on a single trial. All regressors for a single event (e.g. 'Go

odor onset') plotted on the same line to show temporal contiguity, but are fit separately. 'Thirsty' regressor is constantly high throughout a trial when the animal still licks in response to water-predicting odor, and low when the animal is sated. Other regressors are placed within a trial depending on the timing of task events on individual trials. (**D**) Histogram of ratio of total deviance explained (DE) per neuron, for task-modulated vs non-task-modulated neurons. Dashed lines indicate average value for each group. (**E**) Average total DE per cluster, mean ± 95% c.i., using same colors as clusters in Fig 2. (**F**) Per-cluster average DE for other features used in regression. Mean ± 95% c.i. (**G**) Fraction of cells correlated with different variables, and combinations of two variables (State = state; Cue = Go odor onset + No-Go odor onset + Go odor offset + No-Go odor offset; Response = Lick onset + Lick offset), where a cell was correlated with a regressor set if that combination of regressors had > 4% total unique DE. (**H**) Fraction of neurons per-region that are correlated with only one variable (State, Cue, Response), out of total neurons in that region that correlated with any variable or combination of variables. (**I**) Specific selectivity of individual neurons shown by plotting each task-modulated neuron, colored by cluster identity, along axes defined by total unique deviance explained by cue-, response-, and state-related features.

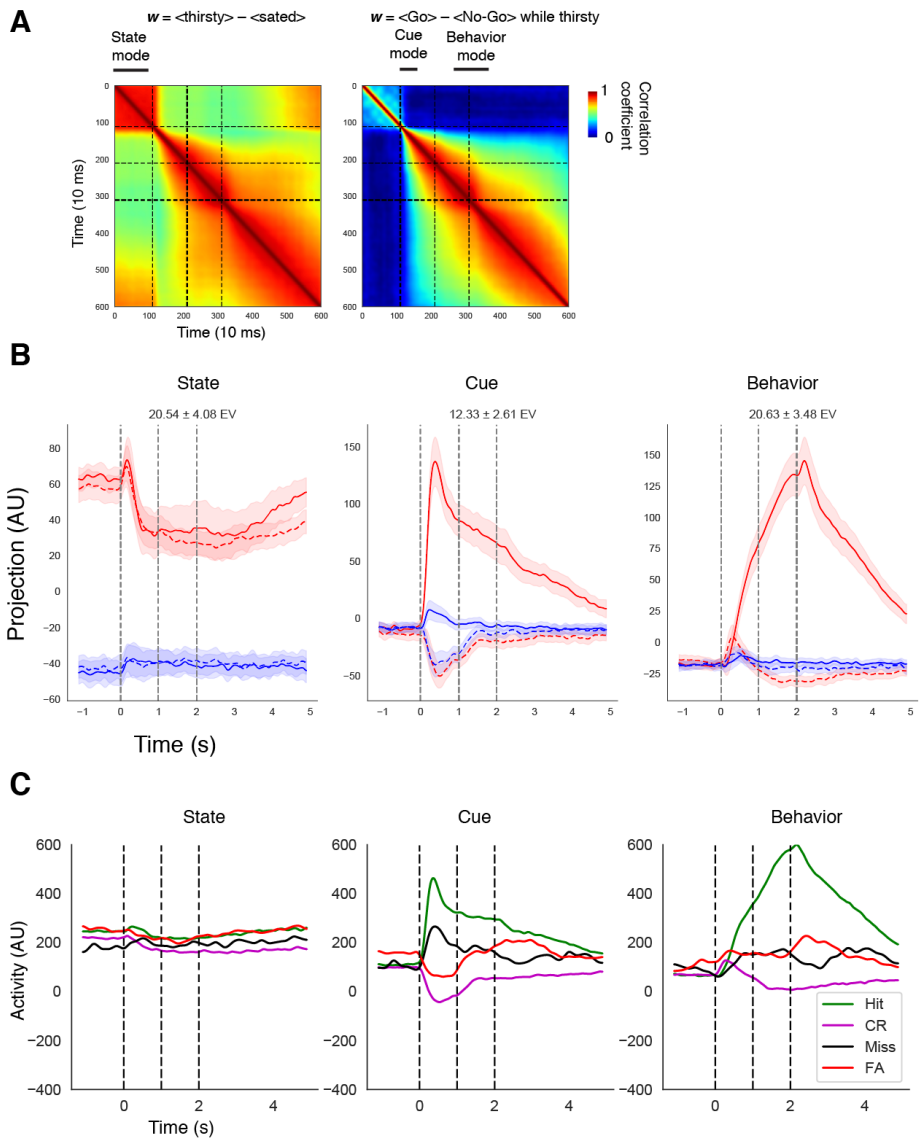

Fig S6: Stability of decoding modes. (**A**) Pearson correlation of ***w*** vector, used to define different activity modes, defined at each 10 ms bin from trial-averaged brain-wide data, with ***w*** vector defined at all other 10 ms bins. Left: ***w*** = <Thirsty> – <Sated>. Right: ***w*** = <Go> – <No Go> while thirsty. High correlations within a time range indicate that the ***w*** vector is stable during that period. (**B**) State, Cue, and Behavior modes computed from randomly subsampled data with the same population size per brain region (20 units per region sampled without replacement from all units in that region across all mice for 1000 repetitions). Mean ± s.d. (**C**) Projections of activity from error trials during the thirsty block defined onto axes defined by Hit and CR trials. Hit = thirsty Go trials where animal obtained reward ('Thirsty Go' elsewhere in paper), CR = Correct rejection = thirsty No-Go trials where the animal withheld licking ('Thirsty No-Go' elsewhere in paper), Miss = thirsty Go trials where the animal did not obtain reward, FA = False Alarm = thirsty No-Go trials where the animal licked during the response epoch. There were often very few error trials per session.

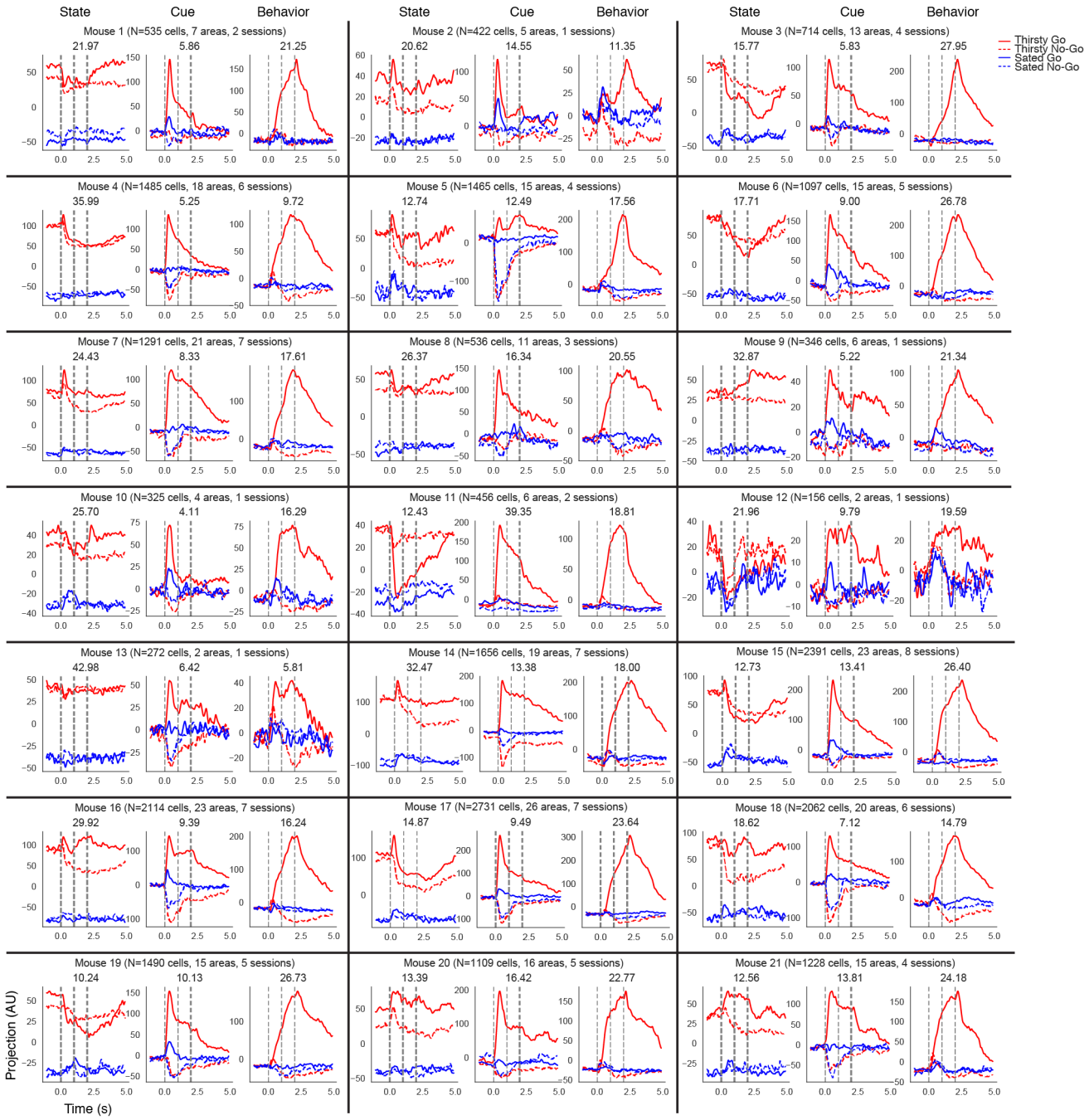

Fig S7. Per-animal projections onto State, Cue, and Response axes. Projections onto State, Cue, and Response axes as Fig 4C, but using only neurons recorded each of the 21 mice. Number above each plot indicates percent task-related explained variance for that mode for that mouse.

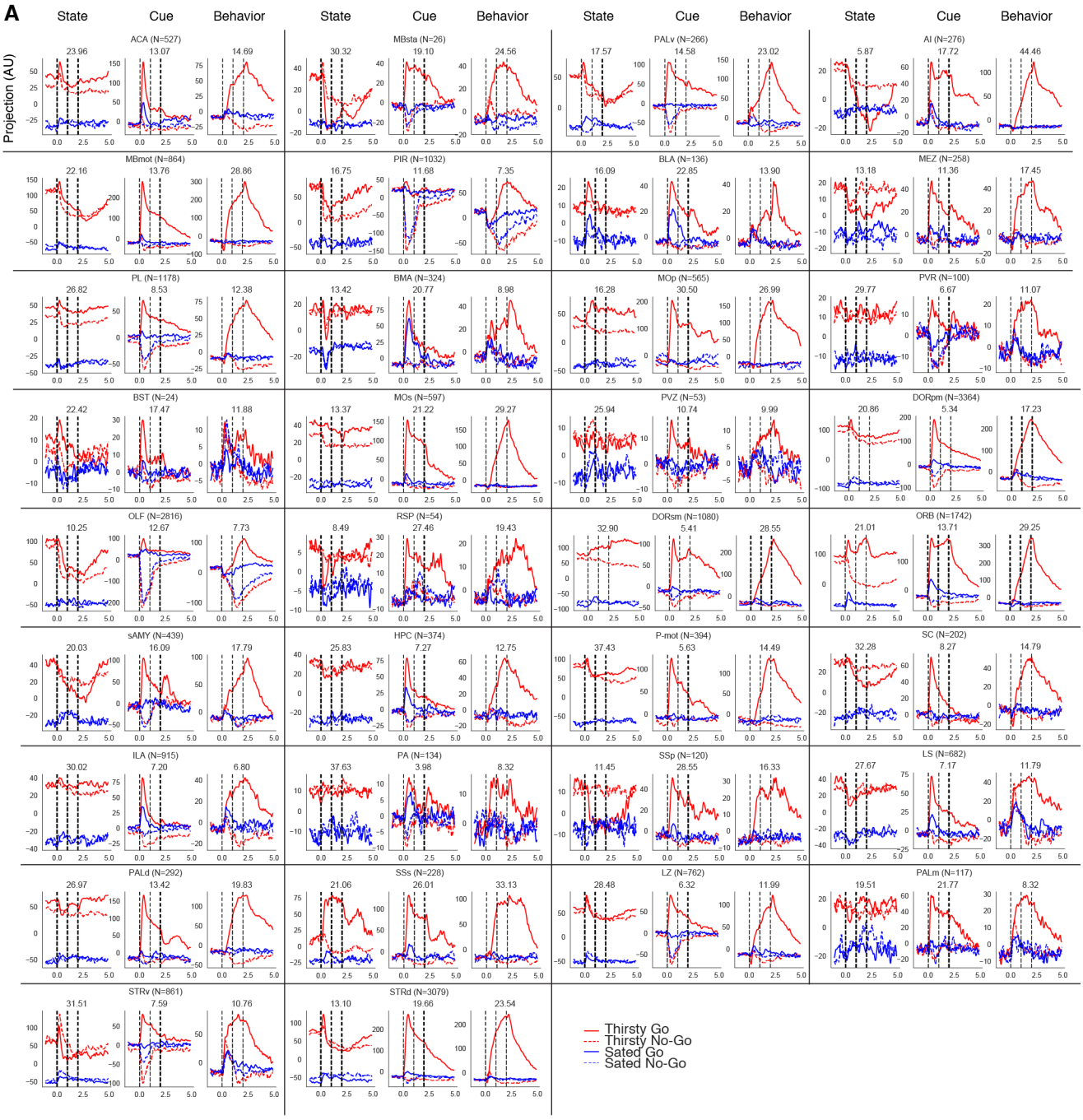
A
State
Cue
Behavior
Projection (AU)
ACA (N=527)
MBsta (N=26)
PALv (N=266)
AI (N=276)
MBmot (N=864)
PIR (N=1032)
BLA (N=136)
MEZ (N=258)
PL (N=1178)
BMA (N=324)
MOp (N=565)
PVR (N=100)
BST (N=24)
MOs (N=597)
PVZ (N=53)
DORpm (N=3364)
OLF (N=2816)
RSP (N=54)
DORsm (N=1080)
ORB (N=1742)
sAMY (N=439)
HPC (N=374)
P-mot (N=394)
SC (N=202)
ILA (N=915)
PA (N=134)
SSp (N=120)
LS (N=682)
PALd (N=292)
SSs (N=228)
LZ (N=762)
PALm (N=117)
STRv (N=861)
STRd (N=3079)
Thirsty Go
Thirsty No-Go
Sated Go
Sated No-Go
B
State Cue Behavior Unexplained
Task-related variance explained
ACA AI BLA BMA BST DORpm DORsm HPC ILA LS LZ MBmot MBsta MEZ MOp MOs OLF ORB P-mot PA PALd PALm PALv PIR PL PVR PVZ RSP SC SSp SSs STRd STRv sAMY

Fig S8: Per-region projections onto State, Cue, and Response axes. (**A**) Per-region State, Cue, and Response mode projections of trial-averaged data, defined in same way as Fig. 4C but only for neurons from a particular brain region (pooled across multiple recordings). Number above each plot indicates percent task-related explained variance for that mode for that region. (**B**) Task-related variance explained by each mode per brain region.

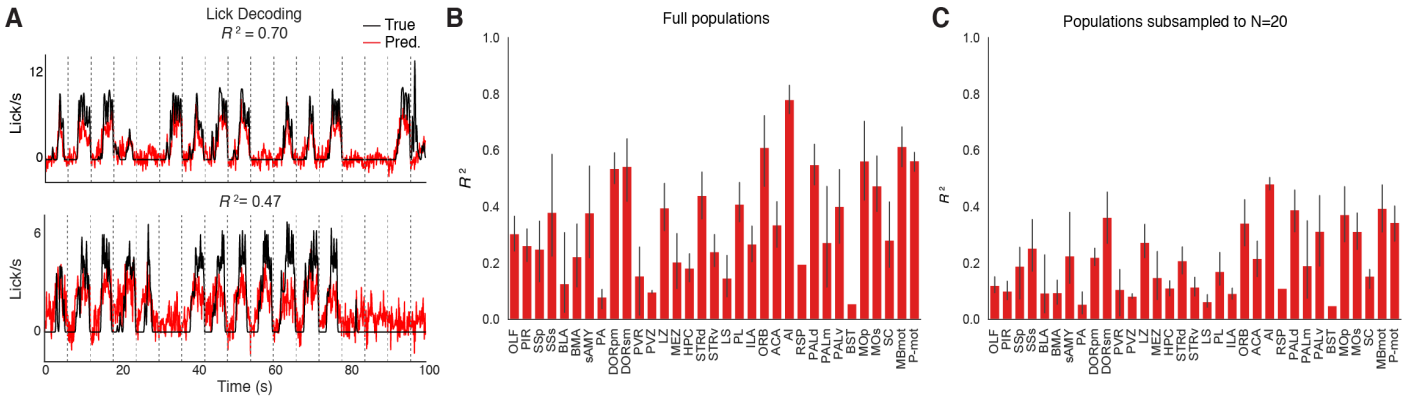

Fig S9: Instantaneous lick rate decoding. (**A**) Examples of continuous lick decoding (100 ms bins). True = observed lick rate. Pred. = predicted lick rate. (**B**) Decoding performance from simultaneously recorded neurons within single brain regions, using full simultaneous population size. (**C**) Decoding performance from simultaneously recorded neurons, using downsampled population size to N=20 neurons (average of 100 random subsamplings per recording session). N per region same as in Fig. 4I-K.

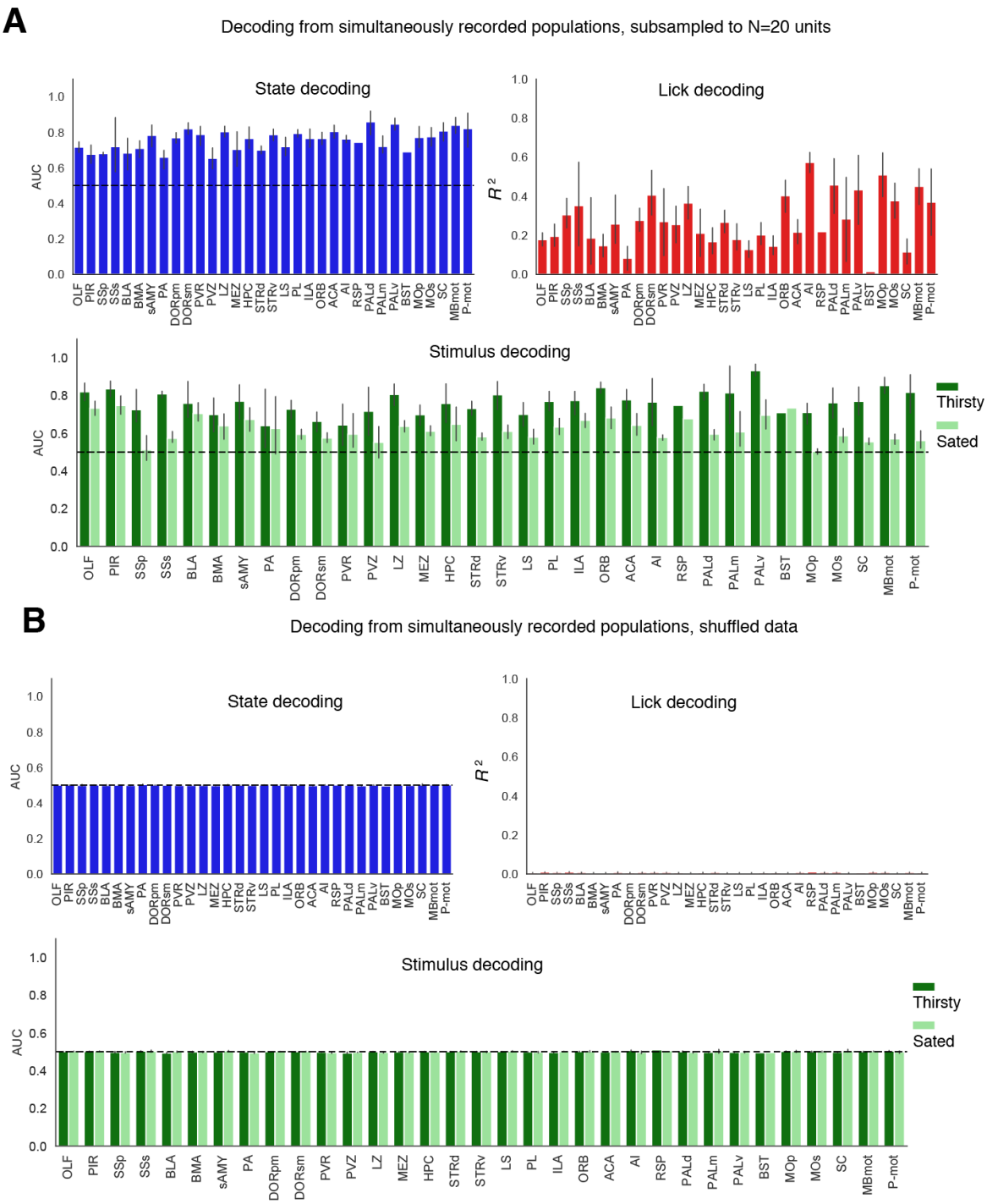

Fig S10: Decoder performance by population size. (**A**) Decoding performance from simultaneously recorded neurons as in Fig 4I-K, but using downsampled population size to *N*=20 neurons (average of 100 random subsamplings per recording session). (**B**) Decoding performance as in Fig 4I-K, but using trial-shuffled data (average of 100 repeats per session). AUC = area under curve. Chance performance (0.5) indicated with dashed line.

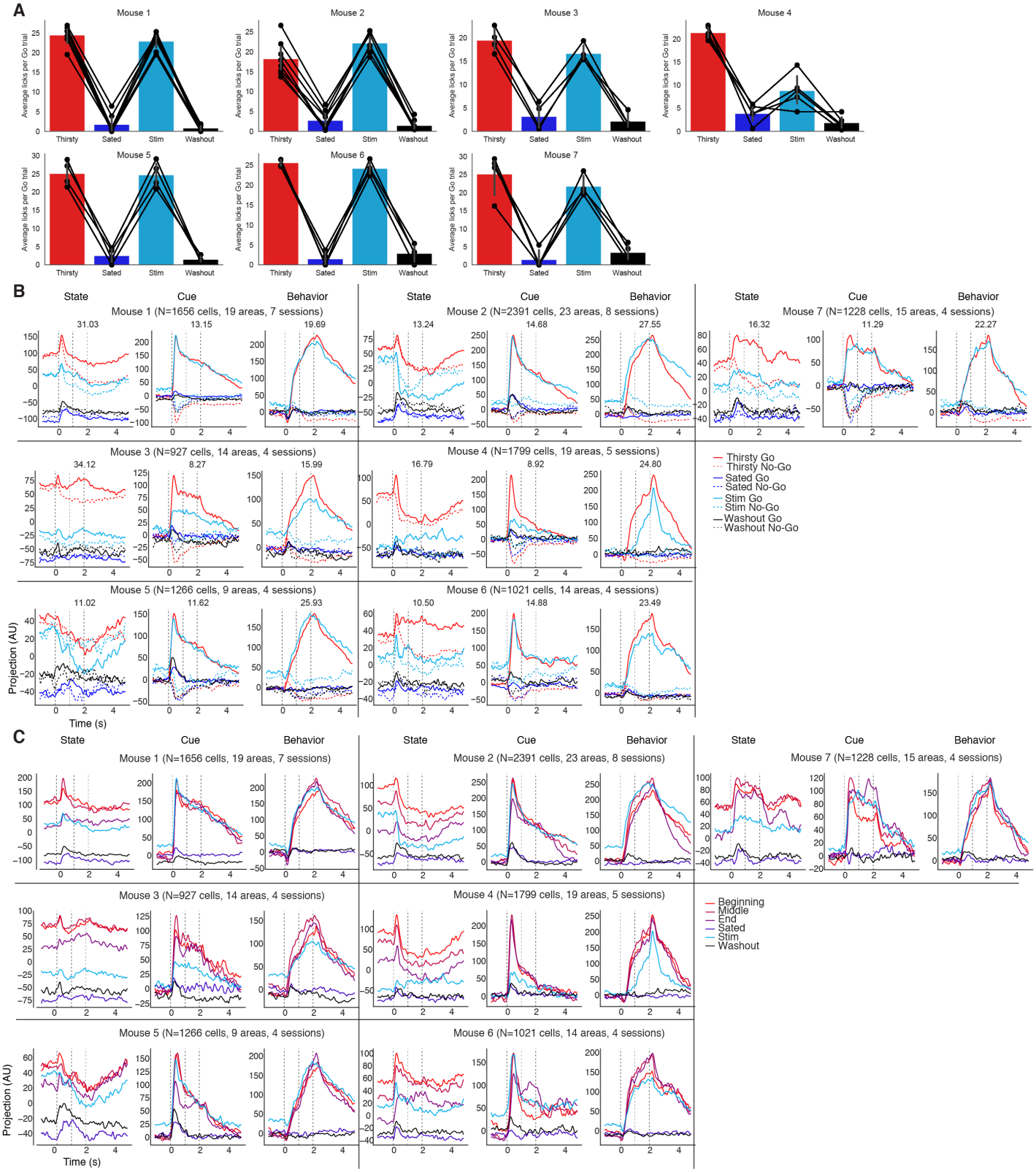
A
Mouse 1
Mouse 2
Mouse 3
Mouse 4
Mouse 5
Mouse 6
Mouse 7
Average licks per Go trial
Thirsty
Sated
Stim
Washout
B
State
Cue
Behavior
Mouse 1 (N=1656 cells, 19 areas, 7 sessions)
Mouse 2 (N=2391 cells, 23 areas, 8 sessions)
Mouse 7 (N=1228 cells, 15 areas, 4 sessions)
Mouse 3 (N=927 cells, 14 areas, 4 sessions)
Mouse 4 (N=1799 cells, 19 areas, 5 sessions)
Mouse 5 (N=1266 cells, 9 areas, 4 sessions)
Mouse 6 (N=1021 cells, 14 areas, 4 sessions)
Thirsty Go
Thirsty No-Go
Sated Go
Sated No-Go
Stim Go
Stim No-Go
Washout Go
Washout No-Go
Projection (AU)
Time (s)
C
Beginning
Middle
End
Sated
Stim
Washout

Fig S11. Per-animal projections onto State, Cue, and Response modes with optogenetic stimulation. (**A**) Per-animal average number of licks per trial while thirsty, sated, and during and after optogenetic stimulation. (**B**) Per-animal projections onto State, Cue, and Response modes (similar to Fig S8), using trial-averaged data from all neurons across all regions recorded in that animal, showing thirsty and sated Go and No-Go conditions. Number above each plot indicates percent task-related explained variance for that mode for that region. (**C**) Same as (B), but showing projections from trials averaged at different stages of satiety on Go trials.

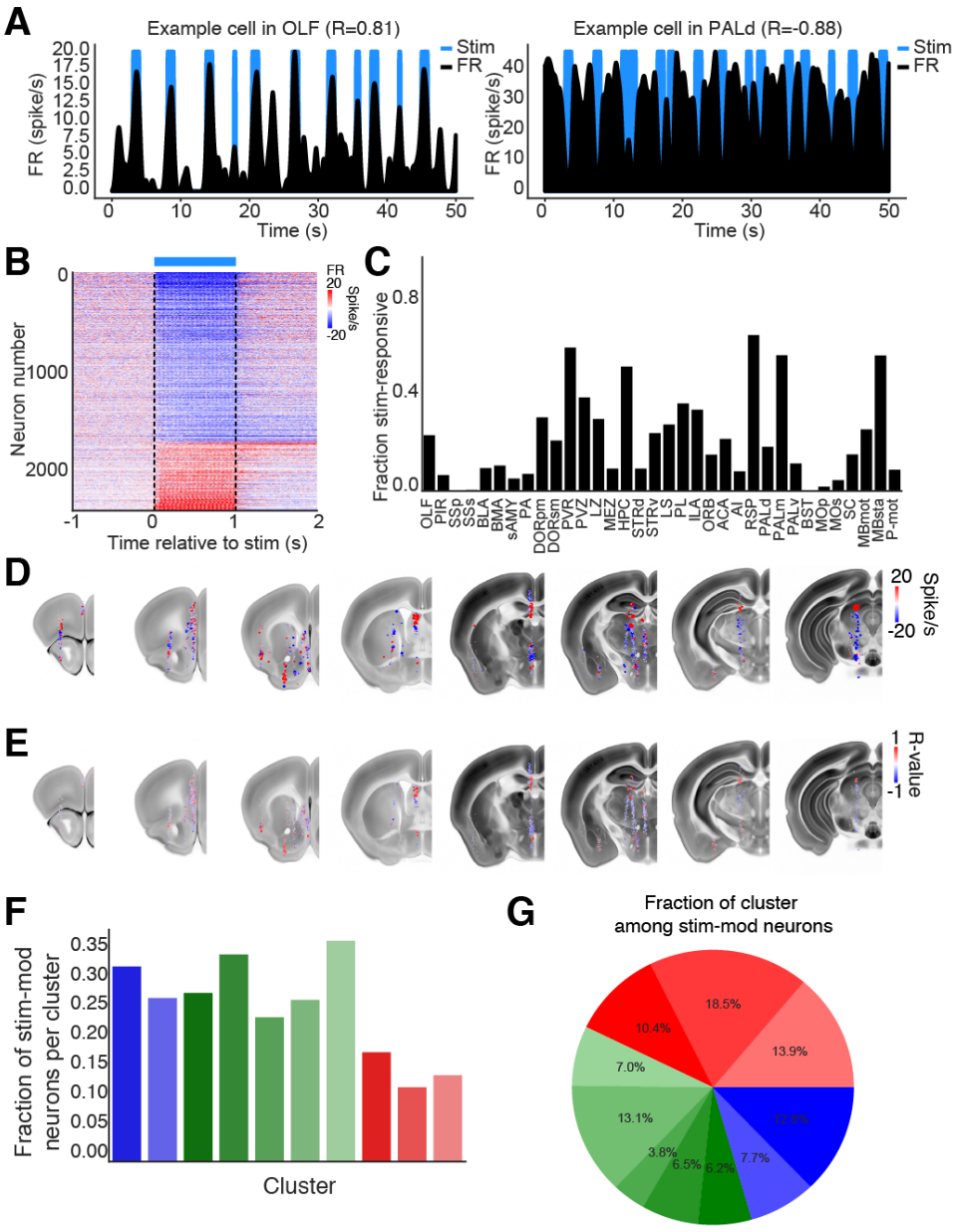

Fig S12: Real-time effects of optogenetic stimulation on downstream neurons. (**A**) Example neurons that are responsive to SFO optogenetic stimulation in OLF and PALd (dorsal pallidum). (**B**) Per-neuron average firing rate around time of 20 Hz optogenetic stimulation (blue band), relative to pre-stimulus firing rate. Neurons are sorted by average change in firing rate within the stimulation period. (**C**) Fraction of stim-responsive neurons per brain region, out of total number of neurons recorded from each region. Stim-response = different firing rate between 1 s preceding stimulus onset and 1 s of 20 Hz stimulation, $P < 0.01$, two-tailed t-test, FDR correction. (**D**) Spatial location of each stim-responsive neuron, colored by average change in firing rate relative to baseline. (**E**) Spatial location of each stim-responsive neuron, colored by correlation with optogenetic stimulus. (**F**) Fraction of neurons per cluster (colors are as defined in Fig 2) that are stim-modulated. (**G**) Fraction of all stim-modulated neurons that come from each cluster.

Table S1
Brain region abbreviations from the Allen Brain Atlas ontology (http://atlas.brain-map.org/)

ACA – Anterior Cingulate cortex	AI – Agranular Insular cortex
BLA – Basolateral Amygdala	BMA – Basomedial Amygdala
BST – Bed Nucleus of the Stria Terminalis	DORpm – Dorsal thalamus, polymodal
DORsm – Dorsal thalamus, sensorimotor	HPC – Hippocampus
ILA – Infralimbic cortex	LS – Lateral Septum
LZ – Lateral zone of the hypothalamus	MBsta – Midbrain, state related
MBmot – Midbrain, motor related	MEZ – Medial zone of the hypothalamus
MOp – Primary motor cortex	MOs – Secondary motor cortex
OLF – Olfactory regions	ORB – Orbitofrontal cortex
P-mot – Pons, motor related	PA – Posterior amygdala
PALd – Dorsal pallidum	PALm – Medial pallidum
PALv – Ventral pallidum	PIR – Piriform cortex
PL – Prelimbic cortex	PVR – Periventricular region
PVZ – Periventricular zone of the hypothalamus	RSP – Retrosplenial cortex
sAMY – Striatal-like amygdalar nucleus	SC – Superior colliculus
SSp – Primary somatosensory cortex	SSs – Secondary somatosensory cortex
STRv – Ventral striatum	STRd – Dorsal striatum

The following lower-level AIBS regions were combined to make the final set of regions used for analysis:

- ACA: [ACAd1, ACAd2/3, ACAd5, ADAd6a, ACAv1, ACAv2/3, ACAv5, ACAv6a, ACAv6b, ACAd6a]
- AI: [AId6a, AIp6a, AIp6b, AIv6a, CLA, GU6a],
- BLA: [BLAa, BLAp, CTXsp],
- BMA: [BMAa, BMAp],
- BST: [BST],
- DORpm: [AD, AMd, AMv, AV, CL, CM, Eth, IAM, IMD, LD, LH, LP, MD, MH, PCN, PF, PO, PT, PVT, RE, RH, RT, SMT, SubG, TH, Xi],
- DORsm: [LGd-co, LGd-ip, LGd-sh, LGv, VAL, VM, VPL, VPLpc, VPM, VPMpc],
- HPC: [CA1, CA2, CA3, DG-mo, DG-po, DG-sg, HPF, ProS, SUB],
- ILA: [ILA1, ILA2/3, ILA5, ILA6a, ILA6b],
- LA: [LA],
- LS: [LSc, LSr, LSv, SF],
- LZ: [FF, HY, LHA, LPO, PSTN, ZI],
- MBmot: [APN, MB, MRN, MT, NOT, PAG, PPT, PR, RN, RR, SNr, VTA],
- MBsta: [PPN, SNc],
- MEZ: [MPN, PH, PMv, PMd, TMv, TU, VMH],
- MOp: [MOp2/3, MOp5, MOp6a, MOp6b],
- MOs: [MOs1, MOs2/3, MOs5, MOs6a, MOs6b],
- OLF: [AON, COApl, COApm, DP, EPd, EPv, NLOT3, OLF, PAA, TTd],

- ORB: [FRP5, FRP6a, ORBl1, ORBl2/3, ORBl5, ORBl6a, ORBm1, ORBm2/3, ORBm5, ORBvl6a],
- P-mot: [PG, PRNc, PRNr, TRN],
- PA: [PA],
- PALd: [GPe, GPi, PAL],
- PALm: [MS, NDB, TRS],
- PALv: [SI],
- PIR: [PIR],
- PL: [PL1, PL2/3, PL5, PL6a, PL6b],
- PVR: [DMH, SBPV],
- PVZ: [PVH, PVHd, PVi],
- RSP: [RSPv2/3, RSPv5, RSPv6a],
- SC: [SCdg, SCdw, SCig, SCiw, SCop],
- SSp: [SSp-n4, SSp-n5, SSp-n6a, SSp-ul6a, SSp-ul6b],
- SSs: [SSs5, SSs6a, SSs6b],
- STRd: [CP, FS, STR],
- STRv: [ACB, OT],
- sAMY: [AAA, CEAc, CEAl, CEAm, IA, MEA]

Caption for Movie S1
Visualization of baseline-subtracted brain-wide activity dynamics, trial-averaged in thirsty and sated Go and No-Go conditions, across the whole brain. Background are coronal sections of Allen Brain Atlas CCv3 autofluorescence brain volume. Coronal plane positions were automatically determined by applying K-means clustering with K=8 to the anterior/posterior coordinates of all recorded units, and using the cluster centroid positions. FR = z-scored firing rate.

References

1. C. Hull, *Principles of Behavior: An Introduction to Behavior Theory* (Appleton-Century, 1943).

2. R. C. Bolles, *Theory of Motivation* (Harper & Row, 1967).

3. F. Toates, *Motivational Systems* (Cambridge Univ. Press, 1986).

4. K. C. Berridge, Motivation concepts in behavioral neuroscience. *Physiol. Behav.* **81**, 179–209 (2004). doi:10.1016/j.physbeh.2004.02.004 Medline

5. S. M. Sternson, A.-K. Eiselt, Three Pillars for the Neural Control of Appetite. *Annu. Rev. Physiol.* **79**, 401–423 (2017). doi:10.1146/annurev-physiol-021115-104948 Medline

6. L. W. Swanson, Cerebral hemisphere regulation of motivated behavior. *Brain Res.* **886**, 113–164 (2000). doi:10.1016/S0006-8993(00)02905-X Medline

7. S. M. Sternson, Hypothalamic survival circuits: Blueprints for purposive behaviors. *Neuron* **77**, 810–824 (2013). doi:10.1016/j.neuron.2013.02.018 Medline

8. M. Fukuda, T. Ono, H. Nishino, K. Nakamura, Neuronal responses in monkey lateral hypothalamus during operant feeding behavior. *Brain Res. Bull.* **17**, 879–883 (1986). doi:10.1016/0361-9230(86)90102-4 Medline

9. M. J. Burton, E. T. Rolls, F. Mora, Effects of hunger on the responses of neurons in the lateral hypothalamus to the sight and taste of food. *Exp. Neurol.* **51**, 668–677 (1976). doi:10.1016/0014-4886(76)90189-8 Medline

10. E. C. O'Connor, Y. Kremer, S. Lefort, M. Harada, V. Pascoli, C. Rohner, C. Lüscher, Accumbal D1R Neurons Projecting to Lateral Hypothalamus Authorize Feeding. *Neuron* **88**, 553–564 (2015). doi:10.1016/j.neuron.2015.09.038 Medline

11. J. Pager, Ascending olfactory information and centrifugal influxes contributing to a nutritional modulation of the rat mitral cell responses. *Brain Res.* **140**, 251–269 (1978). doi:10.1016/0006-8993(78)90459-6 Medline

12. H. D. Critchley, E. T. Rolls, Hunger and satiety modify the responses of olfactory and visual neurons in the primate orbitofrontal cortex. *J. Neurophysiol.* **75**, 1673–1686 (1996). doi:10.1152/jn.1996.75.4.1673 Medline

13. C. R. Burgess, R. N. Ramesh, A. U. Sugden, K. M. Levandowski, M. A. Minnig, H. Fenselau, B. B. Lowell, M. L. Andermann, Hunger-Dependent Enhancement of Food Cue Responses in Mouse Postrhinal Cortex and Lateral Amygdala. *Neuron* **91**, 1154–1169 (2016). doi:10.1016/j.neuron.2016.07.032 Medline

14. Y. Livneh, R. N. Ramesh, C. R. Burgess, K. M. Levandowski, J. C. Madara, H. Fenselau, G. J. Goldey, V. E. Diaz, N. Jikomes, J. M. Resch, B. B. Lowell, M. L. Andermann,

Homeostatic circuits selectively gate food cue responses in insular cortex. *Nature* **546**, 611–616 (2017). doi:10.1038/nature22375 Medline

15. Y. Nakano, Y. Oomura, H. Nishino, S. Aou, T. Yamamoto, S. Nemoto, Neuronal activity in the medial orbitofrontal cortex of the behaving monkey: Modulation by glucose and satiety. *Brain Res. Bull.* **12**, 381–385 (1984). doi:10.1016/0361-9230(84)90109-6 Medline

16. I. E. de Araujo, R. Gutierrez, A. J. Oliveira-Maia, A. Pereira Jr., M. A. L. Nicolelis, S. A. Simon, Neural ensemble coding of satiety states. *Neuron* **51**, 483–494 (2006). doi:10.1016/j.neuron.2006.07.009 Medline

17. C. Gizowski, C. W. Bourque, The neural basis of homeostatic and anticipatory thirst. *Nat. Rev. Nephrol.* **14**, 11–25 (2018). doi:10.1038/nrneph.2017.149 Medline

18. J. N. Betley, S. Xu, Z. F. H. Cao, R. Gong, C. J. Magnus, Y. Yu, S. M. Sternson, Neurons for hunger and thirst transmit a negative-valence teaching signal. *Nature* **521**, 180–185 (2015). doi:10.1038/nature14416 Medline

19. W. E. Allen, L. A. DeNardo, M. Z. Chen, C. D. Liu, K. M. Loh, L. E. Fenno, C. Ramakrishnan, K. Deisseroth, L. Luo, Thirst-associated preoptic neurons encode an aversive motivational drive. *Science* **357**, 1149–1155 (2017). doi:10.1126/science.aan6747 Medline

20. D. E. Leib, C. A. Zimmerman, A. Poormoghaddam, E. L. Huey, J. S. Ahn, Y.-C. Lin, C. L. Tan, Y. Chen, Z. A. Knight, The Forebrain Thirst Circuit Drives Drinking through Negative Reinforcement. *Neuron* **96**, 1272–1281.e4 (2017). doi:10.1016/j.neuron.2017.11.041 Medline

21. V. Augustine, S. K. Gokce, S. Lee, B. Wang, T. J. Davidson, F. Reimann, F. Gribble, K. Deisseroth, C. Lois, Y. Oka, Hierarchical neural architecture underlying thirst regulation. *Nature* **555**, 204–209 (2018). doi:10.1038/nature25488 Medline

22. T. Komiyama, T. R. Sato, D. H. O'Connor, Y.-X. Zhang, D. Huber, B. M. Hooks, M. Gabitto, K. Svoboda, Learning-related fine-scale specificity imaged in motor cortex circuits of behaving mice. *Nature* **464**, 1182–1186 (2010). doi:10.1038/nature08897 Medline

23. W. E. Allen, I. V. Kauvar, M. Z. Chen, E. B. Richman, S. J. Yang, K. Chan, V. Gradinaru, B. E. Deverman, L. Luo, K. Deisseroth, Global Representations of Goal-Directed Behavior in Distinct Cell Types of Mouse Neocortex. *Neuron* **94**, 891–907.e6 (2017). doi:10.1016/j.neuron.2017.04.017 Medline

24. J. J. Jun, N. A. Steinmetz, J. H. Siegle, D. J. Denman, M. Bauza, B. Barbarits, A. K. Lee, C. A. Anastassiou, A. Andrei, Ç. Aydın, M. Barbic, T. J. Blanche, V. Bonin, J. Couto, B. Dutta, S. L. Gratiy, D. A. Gutnisky, M. Häusser, B. Karsh, P. Ledochowitsch, C. M. Lopez, C. Mitelut, S. Musa, M. Okun, M. Pachitariu, J. Putzeys, P. D. Rich, C. Rossant,

W. L. Sun, K. Svoboda, M. Carandini, K. D. Harris, C. Koch, J. O'Keefe, T. D. Harris, Fully integrated silicon probes for high-density recording of neural activity. *Nature* **551**, 232–236 (2017). doi:10.1038/nature24636 Medline

25. C. Stringer *et al*., Spontaneous behaviors drive multidimensional, brain-wide population activity. bioRxiv 306019 [preprint]. 22 April 2018.

26. G. Buzsáki, Large-scale recording of neuronal ensembles. *Nat. Neurosci.* **7**, 446–451 (2004). doi:10.1038/nn1233 Medline

27. M. Rabinovich, R. Huerta, G. Laurent, Transient dynamics for neural processing. *Science* **321**, 48–50 (2008). doi:10.1126/science.1155564 Medline

28. K. V. Shenoy, M. Sahani, M. M. Churchland, Cortical control of arm movements: A dynamical systems perspective. *Annu. Rev. Neurosci.* **36**, 337–359 (2013). doi:10.1146/annurev-neuro-062111-150509 Medline

29. M. Stopfer, V. Jayaraman, G. Laurent, Intensity versus identity coding in an olfactory system. *Neuron* **39**, 991–1004 (2003). doi:10.1016/j.neuron.2003.08.011 Medline

30. O. Mazor, G. Laurent, Transient dynamics versus fixed points in odor representations by locust antennal lobe projection neurons. *Neuron* **48**, 661–673 (2005). doi:10.1016/j.neuron.2005.09.032 Medline

31. M. M. Churchland, J. P. Cunningham, M. T. Kaufman, J. D. Foster, P. Nuyujukian, S. I. Ryu, K. V. Shenoy, Neural population dynamics during reaching. *Nature* **487**, 51–56 (2012). doi:10.1038/nature11129 Medline

32. V. Mante, D. Sussillo, K. V. Shenoy, W. T. Newsome, Context-dependent computation by recurrent dynamics in prefrontal cortex. *Nature* **503**, 78–84 (2013). doi:10.1038/nature12742 Medline

33. M. M. Churchland, B. M. Yu, M. Sahani, K. V. Shenoy, Techniques for extracting single-trial activity patterns from large-scale neural recordings. *Curr. Opin. Neurobiol.* **17**, 609–618 (2007). doi:10.1016/j.conb.2007.11.001 Medline

34. N. Li, K. Daie, K. Svoboda, S. Druckmann, Robust neuronal dynamics in premotor cortex during motor planning. *Nature* **532**, 459–464 (2016). doi:10.1038/nature17643 Medline

35. E. S. Boyden, F. Zhang, E. Bamberg, G. Nagel, K. Deisseroth, Millisecond-timescale, genetically targeted optical control of neural activity. *Nat. Neurosci.* **8**, 1263–1268 (2005). doi:10.1038/nn1525 Medline

36. Y. Oka, M. Ye, C. S. Zuker, Thirst driving and suppressing signals encoded by distinct neural populations in the brain. *Nature* **520**, 349–352 (2015). doi:10.1038/nature14108 Medline

37. C. A. Zimmerman, Y. C. Lin, D. E. Leib, L. Guo, E. L. Huey, G. E. Daly, Y. Chen, Z. A. Knight, Thirst neurons anticipate the homeostatic consequences of eating and drinking. *Nature* **537**, 680–684 (2016). Medline

38. L. Pinto, Y. Dan, Cell-Type-Specific Activity in Prefrontal Cortex during Goal-Directed Behavior. *Neuron* **87**, 437–450 (2015). doi:10.1016/j.neuron.2015.06.021 Medline

39. S. Kato, H. S. Kaplan, T. Schrödel, S. Skora, T. H. Lindsay, E. Yemini, S. Lockery, M. Zimmer, Global brain dynamics embed the motor command sequence of Caenorhabditis elegans. *Cell* **163**, 656–669 (2015). doi:10.1016/j.cell.2015.09.034 Medline

40. M. B. Ahrens, J. M. Li, M. B. Orger, D. N. Robson, A. F. Schier, F. Engert, R. Portugues, Brain-wide neuronal dynamics during motor adaptation in zebrafish. *Nature* **485**, 471–477 (2012). doi:10.1038/nature11057 Medline

41. N. A. Steinmetz, P. Zatka-haas, M. Carandini, K. D. Harris, Distributed correlates of visually-guided behavior across the mouse brain. bioRxiv 474437 [preprint]. 20 November 2018.

42. P. J. Ryan, S. I. Ross, C. A. Campos, V. A. Derkach, R. D. Palmiter, Oxytocin-receptor-expressing neurons in the parabrachial nucleus regulate fluid intake. *Nat. Neurosci.* **20**, 1722–1733 (2017). doi:10.1038/s41593-017-0014-z Medline

43. A. Tsao, J. Sugar, L. Lu, C. Wang, J. J. Knierim, M.-B. Moser, E. I. Moser, Integrating time from experience in the lateral entorhinal cortex. *Nature* **561**, 57–62 (2018). doi:10.1038/s41586-018-0459-6 Medline

44. S. H. Lee, Y. Dan, Neuromodulation of brain states. *Neuron* **76**, 209–222 (2012). doi:10.1016/j.neuron.2012.09.012 Medline

45. D. Sussillo, Neural circuits as computational dynamical systems. *Curr. Opin. Neurobiol.* **25**, 156–163 (2014). doi:10.1016/j.conb.2014.01.008 Medline

46. S. Klein, M. Staring, K. Murphy, M. A. Viergever, J. P. W. Pluim, elastix: A toolbox for intensity-based medical image registration. *IEEE Trans. Med. Imaging* **29**, 196–205 (2010). doi:10.1109/TMI.2009.2035616 Medline

47. L. Ye, W. E. Allen, K. R. Thompson, Q. Tian, B. Hsueh, C. Ramakrishnan, A.-C. Wang, J. H. Jennings, A. Adhikari, C. H. Halpern, I. B. Witten, A. L. Barth, L. Luo, J. A. McNab, K. Deisseroth, Wiring and molecular features of prefrontal ensembles representing distinct experiences. *Cell* **165**, 1776–1788 (2016). doi:10.1016/j.cell.2016.05.010 Medline

48. N. Renier, E. L. Adams, C. Kirst, Z. Wu, R. Azevedo, J. Kohl, A. E. Autry, L. Kadiri, K. Umadevi Venkataraju, Y. Zhou, V. X. Wang, C. Y. Tang, O. Olsen, C. Dulac, P. Osten, M. Tessier-Lavigne, Mapping of Brain Activity by Automated Volume Analysis of

Immediate Early Genes. *Cell* **165**, 1789–1802 (2016). doi:10.1016/j.cell.2016.05.007 Medline

49. M. Pachitariu, N. Steinmetz, S. Kadir, M. Carandini, K. D. Harris, Kilosort: Realtime spike-sorting for extracellular electrophysiology with hundreds of channels. bioRxiv 061481 [preprint]. 30 June 2016.

50. C. Rossant, S. N. Kadir, D. F. M. Goodman, J. Schulman, M. L. D. Hunter, A. B. Saleem, A. Grosmark, M. Belluscio, G. H. Denfield, A. S. Ecker, A. S. Tolias, S. Solomon, G. Buzsáki, M. Carandini, K. D. Harris, Spike sorting for large, dense electrode arrays. *Nat. Neurosci.* **19**, 634–641 (2016). doi:10.1038/nn.4268 Medline

51. E. Z. Macosko, A. Basu, R. Satija, J. Nemesh, K. Shekhar, M. Goldman, I. Tirosh, A. R. Bialas, N. Kamitaki, E. M. Martersteck, J. J. Trombetta, D. A. Weitz, J. R. Sanes, A. K. Shalek, A. Regev, S. A. McCarroll, Highly Parallel Genome-wide Expression Profiling of Individual Cells Using Nanoliter Droplets. *Cell* **161**, 1202–1214 (2015). doi:10.1016/j.cell.2015.05.002 Medline

52. T. Chen, C. Guestrin, in *Proceedings of the 22nd ACM SIGKDD International Conference on Knowledge Discovery and Data Mining* (2016). doi:10.1145/2939672.2939785

53. C. A. Runyan, E. Piasini, S. Panzeri, C. D. Harvey, Distinct timescales of population coding across cortex. *Nature* **548**, 92–96 (2017). doi:10.1038/nature23020 Medline

54. L. N. Driscoll, N. L. Pettit, M. Minderer, S. N. Chettih, C. D. Harvey, Dynamic Reorganization of Neuronal Activity Patterns in Parietal Cortex. *Cell* **170**, 986–999.e16 (2017). doi:10.1016/j.cell.2017.07.021 Medline

55. S. Musall, M. T. Kaufman, S. Gluf, A. Churchland, Movement-related activity dominates cortex during sensory-guided decision making. bioRxiv 308288 [preprint]. 25 April 2018.